Supplementary Information

Orbital selective switching of ferromagnetism in an oxide quasi two-dimensional electron gas

R. Di Capua[1,2], M. Verma[3], M. Radovic[4], V.N. Strocov[4], C. Piamonteze[4], E. B. Guedes[4], N. C. Plumb[4], Yu Chen[2], M. D'Antuono[1,2], G.M. De Luca[1,2], E. Di Gennaro[1,2], D. Stornaiuolo[1,2], D. Preziosi[5], B. Jouault[6], F. Miletto Granozio[2], A. Sambri[2], R. Pentcheva[3], G. Ghiringhelli[7,8] and M. Salluzzo[2]*

[1]*Dipartimento di Fisica "E. Pancini", Università di Napoli "Federico II", Complesso Monte Sant'Angelo via Cinthia, I-80126 Napoli, Italy.*

[2]*CNR-SPIN, Complesso Monte Sant'Angelo via Cinthia, I-80126 Napoli, Italy.*

[3]*Department of Physics and Center for Nanointegration, University Duisburg-Essen Lotharstr. 1, D-47057 Duisburg, Germany.*

[4] *Photon Science Division, Paul Scherrer Institut, CH-5232 Villigen PSI, Switzerland.*

[5] *Université de Strasbourg, CNRS, IPCMS UMR 7504, 67034 Strasbourg, France.*

[6] *Laboratoire Charles Coulomb, UMR 5221, CNRS, Université de Montpellier, F-34095 Montpellier, France*

[7] *Dipartimento di Fisica Politecnico di Milano, Piazza Leonardo da Vinci 32, I-20133 Milano, Italy.*

[8]*CNR-SPIN, Politecnico di Milano, Piazza Leonardo da Vinci 32, I-20133 Milano, Italy.*

Supplementary Note 1. Details of XAS and XMCD analysis and supplementary data.

1.1 X-ray Absorption Spectroscopy and X-ray magnetic linear and circular dichroism experiment

X-ray Absorption spectra have been acquired using Total Electron Yield (TEY) method. The x-ray magnetic circular dichroism technique allows determining the projection of the magnetic moment associated to a specific ion in the structure along the photon beam direction. The circular polarization of the light carries a moment, which is transferred to the absorbing atom. Selection rules imply different XAS spectra for the two opposite (left and right) circular polarizations if the absorbing ion is characterized by a magnetic moment component along the beam direction.

In the TEY mode we measure a current that is proportional to the photo and Auger electrons created by the photo-absorption process. However, only the photo and Auger electrons created within the electron escape depth reach the surface after elastic and inelastic collisions. Overall, neutrality requires a current of electrons going from the ground to the sample. By measuring this current, we get a measure of the electrons leaving the samples. The electron escape depth is few nm's, and in the particular case of absorption from Ti-$L_{2,3}$ edge, it is of the order of 2-3 nm.

In the case of transition metal oxides and for soft x-ray absorption processes, i.e. 2p->3d transition, sum rules can be applied to get a quantitative estimate of the effective spin (m_{Espin}) and orbital components (m_{orb}) of the magnetic moment. However, as discussed in details in ref. (25) of the main text, the application of the sum rules is powerful but needs some care in particular for light transition metals, like titanium.

The equations to be used are the following:

$$m_{Espin} = \frac{6\int_{L_3}(I^+ - I^-)dE - 4\int_{L_3+L_2}(I^+ - I^-)dE}{\int_{L_3+L_2}(I^+ + I^-)dE}(10 - n_{3d}) \quad (1)$$

$$m_{orb} = -\frac{4\int_{L_3+L_2}(I^+ - I^-)dE}{3\int_{L_3+L_2}(I^+ + I^-)dE}(10 - n_{3d}) \quad (2)$$

where I^+ and I^{-} are the XAS spectra acquired with the two circular polarizations, the magnetic dichroism is XMCD=$I^+ - I^-$, and n_{3d} is the 3d electronic density. To evaluate eq. (1) it is necessary to separate the L_3 and L_2 edges in the experimental spectrum and calculate the following integrals:

$$p = \int_{L_3} (I^+ - I^-) dE \tag{3}$$

$$q = \int_{L_3+L_2} (I^+ - I^-) dE$$

However, the L_3 and L_2 contributions are substantially mixed in the Ti XAS spectra. Thus, the evaluation of the spin moment at Ti-edge is affected by large error. The spin moment obtained from the sum rules could be underestimated by a factor of 4, roughly. On the other hand, the orbital moment can be calculated safely, since there is no need to separate the integrals at the L_2 and L_3 edges and the relationship between the orbital moment and the XMCD is exact. From this analysis we find at saturation m_{orb}=-0.045 μ_B/Ti. We have also applied the spin sum rule with the aim of obtaining an order of magnitude estimate of the spin moment. This gives m_{spin}=0.07 μ_B/Ti, thus a total magnetic moment of the order of 0.02-0.03 μ_B/Ti.

1.2 Comparison between DFT+U calculated Ti-magnetic moment and experimental results.

In order to evaluate the value of the Ti-magnetic moment which we should expect from the outcome of the Ti-XMCD analysis on the basis of the layer resolved DFT+U calculations, we need to take into account the finite probing depth of Total Electron Yield (TEY). The expression of the Total Electron Yield (TEY) signal coming from a multilayer can be found in several textbooks.

The Auger electron current emitted from atoms within the solid angle Ω of the element A in the n-th layer (placed between depths z_n and z_{n+1}) is:

$$I(z_n) = k_{nA} \int_{\Omega} \int_{z_n}^{z_{n+1}} exp\left(-\frac{z}{d} cos\alpha\right) d\Omega dx \quad (4)$$

where k_{nA} is proportional to the primary electron beam current and to a coefficient determining the Auger electron emission, α is the incidence angle and d is the Auger electron Inelastic Mean Free Path (IMFP) in the sample.

With simple integration, it turns out that contribution to the total magnetic moment measured from a layer placed between depths $z_n = na$ and $z_{n+1} = (n+1)a$ (with a the lattice constant) is:

$$M(z_n) = m_n e^{-\frac{na}{d}} \left(1 - e^{-\frac{(n+1)a}{d}}\right) \quad (5)$$

where m_n is the Ti-magnetic moment of the layers.

Thus, the total Ti-magnetic moment which we should expect from the outcome of the Ti-XMCD analysis, is:

$$M = \sum_n m_n e^{-\frac{na}{d}} \left(1 - e^{-\frac{(n+1)a}{d}}\right) \quad (6)$$

By replacing m_n with the Ti-magnetic moment of each layer as obtained from DFT+U calculations, we find a magnetic moment of 0.05 μ_B/Ti assuming d=2 nm, and 0.035 μ_B/Ti if d=3 nm. These values are in good overall agreement with the estimated magnetic moment from the XMCD analysis.

1.3 X-ray Multiple scattering calculations and charge transfer

Simulations including charge transfer (CT) effects were done using charge transfer ligand field multiplet theory, implemented in the CTM4XAS software (ref. 23 of the main

text). The CT is included in an Anderson impurity type of model where two parameters are necessary to describe the system: the energy difference between the Ti-*3d* and the ligand band (called Δ here), and the transfer integral which describes the overlap between metal and ligand bands and therefore gives the probability for the electron to be transferred. The Δ fitting the XAS data is 4 eV. The transfer integrals used were 2 and 1 for b_1, a_1 (d_{x2-y2}, d_{z2}) and b_2, e (d_{xy}, d_{xz}/d_{yz}) orbitals, respectively. This choice is commonly used for octahedral or close to octahedral systems and the reasoning behind is that the probability for electron transfer is higher (in this case two times higher) for orbitals pointing in the bond direction, as d_{x2-y2}, d_{z2}. We used U_{pd}-U_{dd}=2eV. The crystal field parameters were $10D_q$=2.3, D_s=-0.02, D_t=-0.002. A slightly larger value of $10D_q$ compared to the simulation for LAO/STO seems to fit better the energy difference between the double peaks at L_3 and L_2 edges. The Slater Integrals were reduced by 90% applied on the corrected Hartree-Fock values. This simulation gives a number of 3d holes equals to 9.65. The broadening used were 0.1 eV for the Gaussian broadening, to account for the energy resolution, and different Lorentzian broadening for each of the 4 peaks of the spectrum, namely half width at half maximum of 0.11 eV, 0.34 eV, 0.5 eV, and 0.65 eV for the four XAS peaks (from the first to the last).

Supplementary Figure 1 shows the comparison of the simulation with LAO/ETO/STO XAS data. The XAS data agreement is very good, except for the features around 470 eV and 475 eV.

In Supplementary Figure 2 we also show simulation for titanium in a Ti^{3+} configuration in D4h symmetry, which is reminiscent of the shape of Constant Initial State (CIS) spectra obtained by integrating the valence band RESPES results shown in Fig. 3b of the main text. We used the same crystal field splitting parameters employed for Ti^{4+} spectra and the same CT parameters. The charge transfer has the effect of increasing the valleys between the peaks. In the simulations shown below we have also plotted different simulated spectra as function of the 10Dq value from 1.0 eV to 2.1 eV.

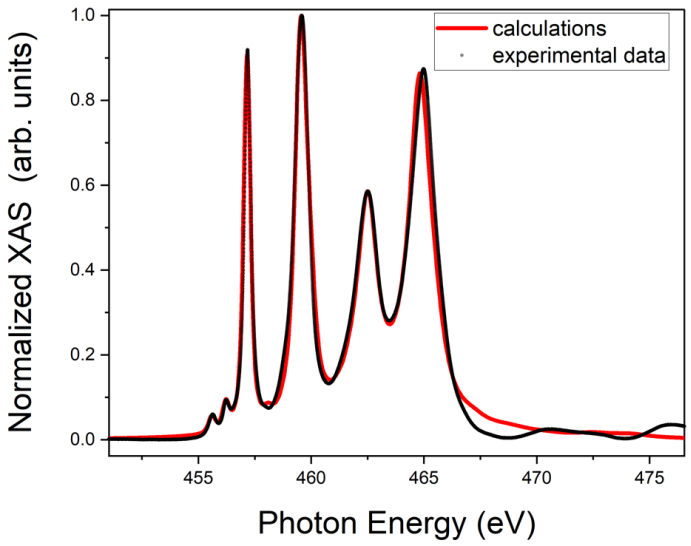

Supplementary Figure 1: Atomic multiplet splitting simulation of the XAS spectra of Ti^{4+} systems. Typical TEY Ti-$L_{2,3}$ edge XAS spectrum on LAO/ETO/STO system in C+ polarization (black circles) and atomic multiplet atomic splitting simulation (red line).

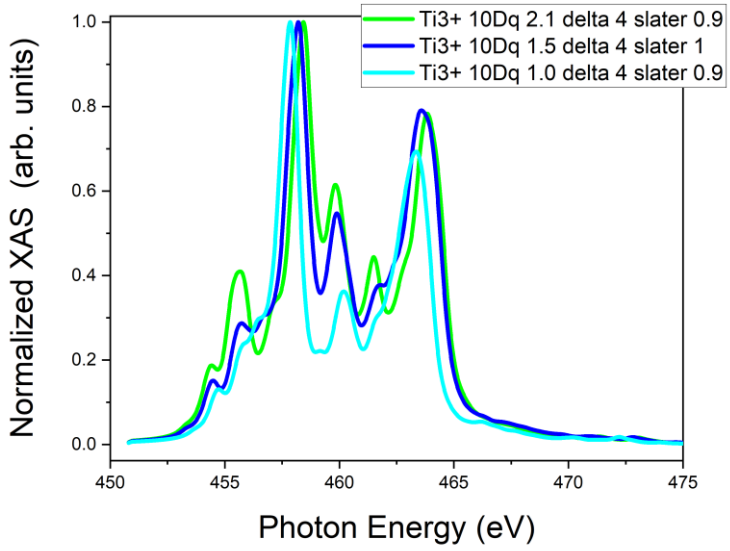

Supplementary Figure 2: Atomic multiplet splitting simulation of the XAS spectra of Ti^{3+} systems. Atomic multiplet splitting simulation assuming Ti^{3+} valence state with varying crystal field (10 Dq) parameters.

Supplementary Note 2. Analysis of the anomalous Hall effect

The non-linear, ordinary, Hall effect usually observed in LAO/STO heterostructures above the Lifshitz transition, is related to the presence of two bands with different carrier densities and mobilities. It can be fitted using the following expression:

$$R_{xy}^{OHE}(\mu_0 H) = -\frac{B}{e}\frac{\frac{n_1\mu_1^2}{1+\mu_1^2B^2}+\frac{n_2\mu_2^2}{1+\mu_2^2B^2}}{\left(\frac{n_1\mu_1}{1+\mu_1^2B^2}+\frac{n_2\mu_2}{1+\mu_2^2B^2}\right)^2+\left(\frac{n_1\mu_1^2}{1+\mu_1^2B^2}+\frac{n_2\mu_2^2}{1+\mu_2^2B^2}\right)^2B^2} \quad (7)$$

with n_1, μ_1, n_2, μ_2 the 2D carrier densities and the mobilities of the two bands, and $B = \mu_0 H$. The parameters in eq. (7) have the constraint $1/R_s = e(n_1\mu_1 + n_2\mu_2)$, where R_s is the sheet resistance. In Supplementary Figure 3a, b we report the R_{xy} data on sample B of Fig. 2 in the main text. The data were acquired at high gate voltage (V_g=+30V) and at different temperatures above and below the FM T_c, (T=20K (Fig. 3a) and T=2K (Fig. 3b)). In Supplementary Figure 3c, d we plot the corresponding derivative curves, $dR_{xy}/d\mu_0 H$. Red Lines in panels a,c are fitting curves using eq.(7). One can notice that the derivative of the data measured at 20K (Fig. 3c) shows a minimum at zero field. The data at T=2K in Fig. 3d, instead, show a peak at $\mu_0 H = 0$ and a minimum around 5T. The change from decreasing to increasing derivative in Fig. 3d points to the presence of two curvatures in the R_{xy} data: a downward curvature at low field (<4T) and an upward curvature at high field (>6T). The latter is due to the emergence of the second band contribution in the Hall effect, similarly to what happens in Fig. 3c; while the former is due to AHE. Thus, in the spin-polarized q2DEG at 2K, the Hall effect is given by two terms, the ordinary Hall effect $R_{xy}^{OHE}(\mu_0 H)$ (eq.7) and the AHE term $R_{xy}^{AHE}(\mu_0 H) \propto \rho_{AHE} M_z(\mu_0 H)$, where ρ_{AHE} is the anomalous 2D resistivity at saturation, and $M_z(\mu_0 H)$ is the magnetization.

In order to isolate the AHE contribution and estimate the ρ_{AHE} parameter, we identify the field interval above the saturation of the magnetization and below the activation of the

two bands transport, as that corresponding to the minimum of the $dR_{xy}/d\mu_0 H$ curve. In this

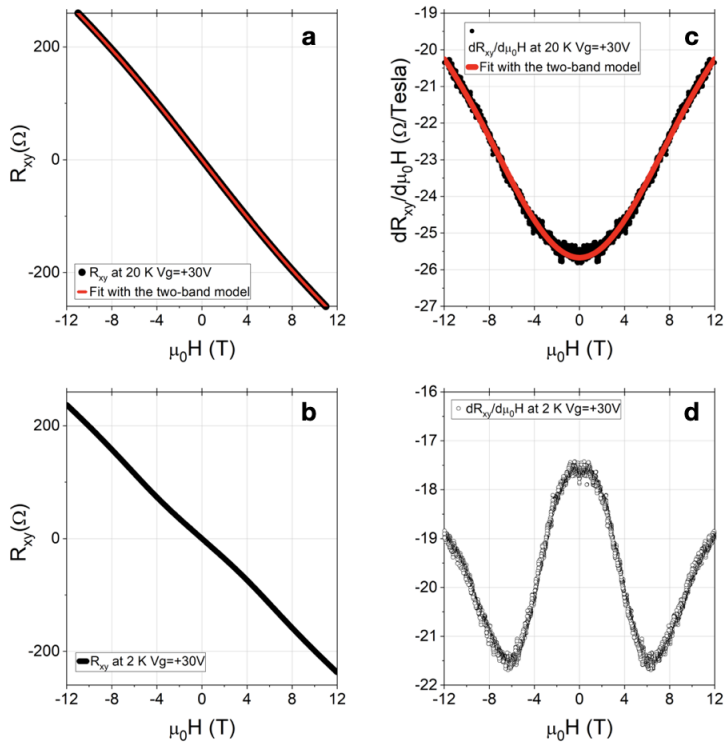

Supplementary Figure 3: Analysis of the Hall effect and fit. Two band fit (red line) of (a) R_{xy} and (c) $dR_{xy}/d\mu_0 H$ Hall effect data at 20 K (circles). (b) R_{xy} and (d) $dR_{xy}/d\mu_0 H$ on the same sample at 2K.

interval R_{xy} is almost linear and a slope, having the value of the $dR_{xy}/d\mu_0 H$ in that point, can be subtracted to the data. The resulting Hall effect profile shows a plateau corresponding to the 2D anomalous resistivity at saturation ρ_{AHE}, that extends up to the field at which the second band starts to contribute, as can be seen in Supplementary Figure 4a (black line). The anomalous 2D resistivity ρ_{AHE} determined in this way corresponds also to the intercept of the linear slope to zero field, as shown by the red dashed lines in Fig. 2 of the main text.

In order to verify that the procedure followed to evaluate the anomalous Hall component is correct, we report an analysis of the $R_{xy} - R_{xy}^{AHE}(\mu_0 H)$ vs. $\mu_0 H$ data in the full field range, i.e. the Hall effect data after subtraction of the anomalous contribution. Firstly, we

extrapolate the $R_{xy} - R_{xy}^{AHE}(\mu_0 H)$ curve up to the maximum field value (red line in Supplementary Figure 4a), then we subtract this data from the R_{xy} data. The resulting

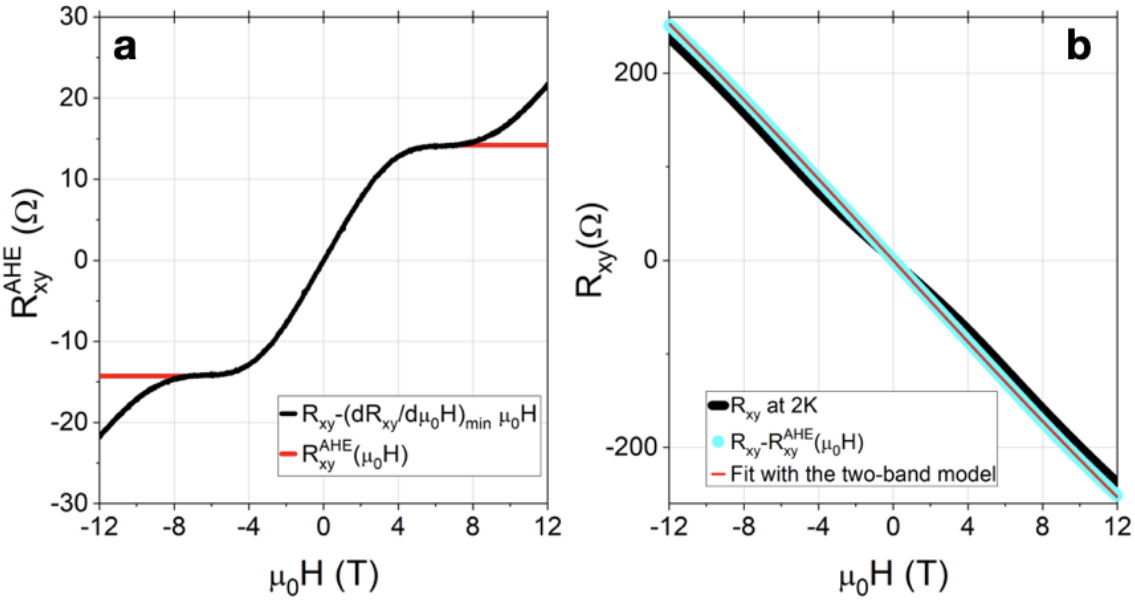

Supplementary Figure 4 (a) Curve obtained after subtraction of a linear slope from the R_{xy} of sample B at 2K (black line) and $R_{xy}^{AHE}(\mu_0 H)$ obtained by extrapolating to the saturation value. (b) R_{xy} (black line) and $R_{xy} - R_{xy}^{AHE}(\mu_0 H)$ vs. $\mu_0 H$ (cyan scatter data) and two-band fit (red line). Fit parameters obtained at 2K are: low mobility band, 2D carrier density n_1 = 2.4 10^{13} cm^{-2} and mobility μ_1 = 275 $cm^2V^{-1}s^{-1}$; high mobility band n_2 =1.3 10^{13} cm^{-2} and μ_2 =900 cm^2 V-1s^{-1}. At 20 K the two-band fitting parameters are similar, namely: 2D carrier density n_1 = 2.5 10^{13} cm^{-2} and mobility m_1 = 278 $cm^2V^{-1}s^{-1}$; high mobility band n_2 =1 10^{13} cm^{-2} and μ_2 =920 cm^2 $V^{-1}s^{-1}$.

curve is shown in Supplementary Figure 4b in cyan. This curve, devoid of the anomalous contribution, can now be fit using the pure two-band model of eq. (7), with fitting parameters similar to those obtained at 20 K. This example of analysis of our Hall effect data show that the method employed gives consistent results.

Supplementary Note 3. Band-dispersion data and tight binding fit.

In Supplementary Figure 5 we show band-dispersion data acquired with different polarization along with their analysis. It is worth noting that, beside the main conduction bands, our data reveal also a replica band about 150-190 meV below the Fermi level, which were already observed in q2DEGs of STO (ref. [30] of the main text) and LAO/STO (ref. [33] of the main text) at low/intermediate doping, and attributed to a signature of large polarons associated to a strong coupling between LO3 optical phonons and carriers. ETO and STO are characterized by LO3 optical phonons at similar energies, thus the data suggest that, alike LAO/STO and STO, also in LAO/ETO/STO heterostructures, at a low/intermediate doping level, quasiparticles are large polarons.

The band-dispersion profiles were analyzed by combining the spectra acquired with different polarizations, and by fitting the Momentum Dispersion Curves (MDC) as function of the energy relative to the Fermi level E_F. Finally, the band profiles were compared to the two-dimensional(2D) curvature maps of the raw data (ref. 35 of the main text), as further validation of the fitting process for the band identification.

Circular polarization (C+) E vs. k_x and dispersions include features associated to all the bands in the system, namely bands with $3d_{xz}$, $3d_{yz}$ and $3d_{xy}$ orbital characters; dataset recorded in *p-pol* configuration are mainly affected by the $3d_{xz}$ band, while *s-pol* configuration provides information about the $3d_{xy}$ and the $3d_{yz}$ bands (d_{xy} indicates the light band, while d_{xz} and d_{yz} refer to the heavy bands along the short and the long diameters of the ellipse, respectively).

We assumed for simplicity three independent two-dimensional bands as described by eqs. (8)-(10):

$$E_{xy}(k_x, k_y) - E_F = 2V_{xy}(2 - cosk_x a_0 - cosk_y a_0) + E_{0xy} \quad (8)$$

$$E_{xz}(k_x, k_y) - E_F = 2V_{xz}(1 - cosk_x a_0) + 2V_{yz}(1 - cosk_y a_0) + E_{0xz} \quad (9)$$

$$E_{xz}(k_x, k_y) - E_F = 2V_{yz}(1 - cosk_x a_0) + 2V_{xz}(1 - cosk_y a_0) + E_{0yz} \quad (10)$$

where a_0 is the lattice constant V_{xy}, V_{xz}, V_{yz} are the hopping parameters or so-called inner potentials, which determine the band-curvatures and the effective masses, E_F is the Fermi energy, and E_{0xy}, E_{0xz}, E_{0yz} are the $E - E_F$ value at k_x , k_y= 0, i.e. the band bottom of each band (E_{0xz} and E_{0yz} are expected to have the same value inside the experimental error).

In our experimental configuration, recorded maps correspond to E vs. k_x curves at $k_y = 0$, so that the above equations read as:

$$E_{xy}(k_x) - E_F = 2V_{xy}(1 - cosk_x a_0) + E_{0xy} \quad (11)$$

$$E_{xz}(k_x) - E_F = 2V_{xz}(1 - cosk_x a_0) + E_{0xz} \quad (12)$$

$$E_{xy}(k_x) - E_F = 2V_{yz}(1 - cosk_x a_0) + E_{0yz} \quad (13)$$

The experimental E vs. k_x datasets are obtained by deconvolving MDC intensity profiles of ARPES maps as superposition of Lorentzian contributions. The MDC profile corresponding to a given $\varepsilon = E - E_F$ value is obtained by averaging ARPES intensity values at each k_x over an energy window of 10 meV (centered on the chosen energy). At each given ε value, the central k_x of each Lorentzian contribution defines the (k_x, ε) point to be employed in the tight binding fitting procedure through eqs. (11)-(13).

The inferred (k_x, ε) points overlapped to ARPES maps (recorded at different polarizations of the incident photons) and to the 2D curvature map in C+ polarization, together with the band profiles as obtained from the fit procedure, are reported in Supplementary Figure 5. In the same figure, MDC profiles with their multiple Lorentzian fit are also shown; such Lorentzian deconvolutions provide the experimental points to be employed for the tight binding fit of the bands. For each experimental point, the error bar on the binding energy (vertical scale) is taken as the window of integration used to estimate the MDC curves (10 meV), while the error on the momentum (horizontal scale) is determined from the sensitivity of the corresponding Lorentzian deconvolution.

Finally, the error in the effective masses is determined by propagating the uncertainties associated to the estimation of the Fermi momentum and of the band bottoms of each band, as inferred from the tight binding fits.

In Table 1 we report all the parameters estimated from the fit.

Supplementary Table 1. Fitting parameters of the MDC data.

V_{xy} (eV)	V_{yz} (eV)	V_{xz} (eV)	E_{0xy} (meV)	E_{0xz}/E_{0yz} (meV)	$k_{F\,(xy)}$ (Å^{-1})	$k_{F\,(yz)}$ (Å^{-1})	$k_{F\,(xz)}$ (Å^{-1})
0.70±0.05	0.050±0.005	1.10±0.05	-85±5	-50±5	0.09±0.01	0.27±0.02	0.055±0.005

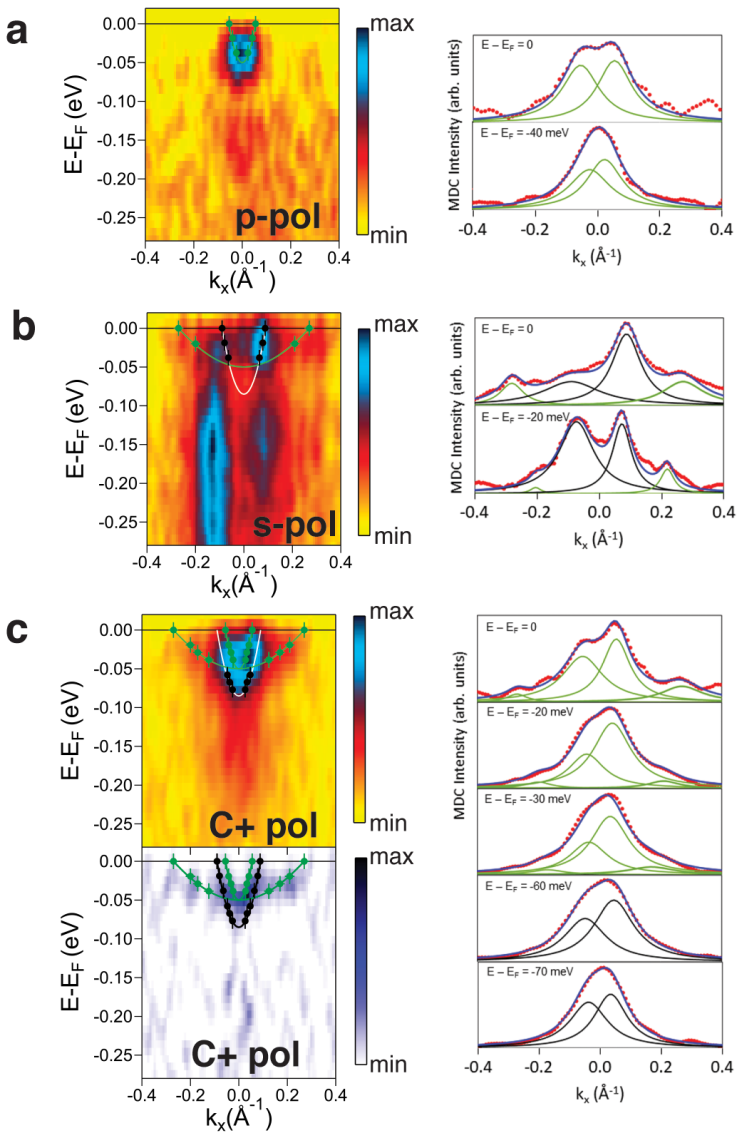

Supplementary Figure 5: Left panels: Band dispersion ARPES maps recorded with (a) p, (b) s, and (c) C+ polarizations of incident photons in the 2nd Bz. In panel (c) we show also the corresponding 2D curvature map of the C+ data. Right panels: some MDCs profiles at different binding energies (scatter data) extracted from each map and their Lorentzian deconvolutions as described in the text. The experimental points inferred from the deconvolution of the MDCs (black: d_{xy} "light" band; green: d_{xz} and d_{yz} "heavy" bands), as well as the tight binding best fit curves, are overlapped to the ARPES and curvature maps. Only points that could be clearly detected in the deconvolution and assigned were employed. The curves reported on different maps corresponding to the same band were estimated by a joint fit on all the points evaluated on the different maps.

Supplementary Note 4. Supplementary DFT+U calculations

In Supplementary Figure 6 we show the effect of the Hubbard U for Ti-3d states on the band structure calculations in the (FM) ground state of (001) LAO/ETO/STO (U=2eV and U=4eV). We used the same c(2x2) setup described in the main text. We show here the calculations on both large (upper panels) and small (bottom panels) energy range around E_F. Theory predicts several non-spin-polarized bands in the -1.5 eV to E_F binding energy range deriving from the LAO contribution to the density of states, including a (hole-) band (green line in the figure) crossing the Fermi level associated with the AlO_2 surface state (LAO SS). The LAO related bands are not observed in the RESPES data, in agreement with previous studies on standard LAO/STO interfaces (refs [31]-[33] of the main text), indicating that the LAO exposed surface is not ideal and can be passivated by adsorbates, in particular after ambient exposure.

One can see that the value of U of Ti-3d has an effect on the position of the Eu-4f peak, which shift to lower energy, around -1.6 eV for U=2eV, against the experimental value of -2 eV which is in very good agreement with the simulation done with *U*=4 eV. Moreover, the Ti-*3d U*-value also has an effect on the band dispersions and on the FM splitting. The latter is reduced by still sizeable for *U*=2eV, thus a FM ground state is a very robust outcome of DFT+U calculations. Furthermore, the bottom of the lowest band, having a $3d_{xy}$ orbital character, is shifted to lower energy in the U=2eV case, and the $3d_{xz}/3d_{yz}$ heavy band is shifted to higher energy. Both results give a splitting at Γ which is sensitively different from the experimental result (in both the FM and AFM (not shown) solution). Thus, from the analysis of the effect of the Ti-3d Hubbard U we conclude that a better agreement with the experimental results is obtained assuming *U*=4eV. On the other hand, the main result, i.e. the FM-ground state of the system, is independent on the choice of the *U*-value.

In Fig. 7 we show the layer resolved LDOS and magnetic moment for a setup with an increased number of STO layers (10.5 and 14.5). The calculations confirm that the 2DEG is confined within the first 3 uc of STO and that the Ti-magnetic moment is present in ETO and in the first 3uc of STO, i.e. in the region where the 2DEG is confined.

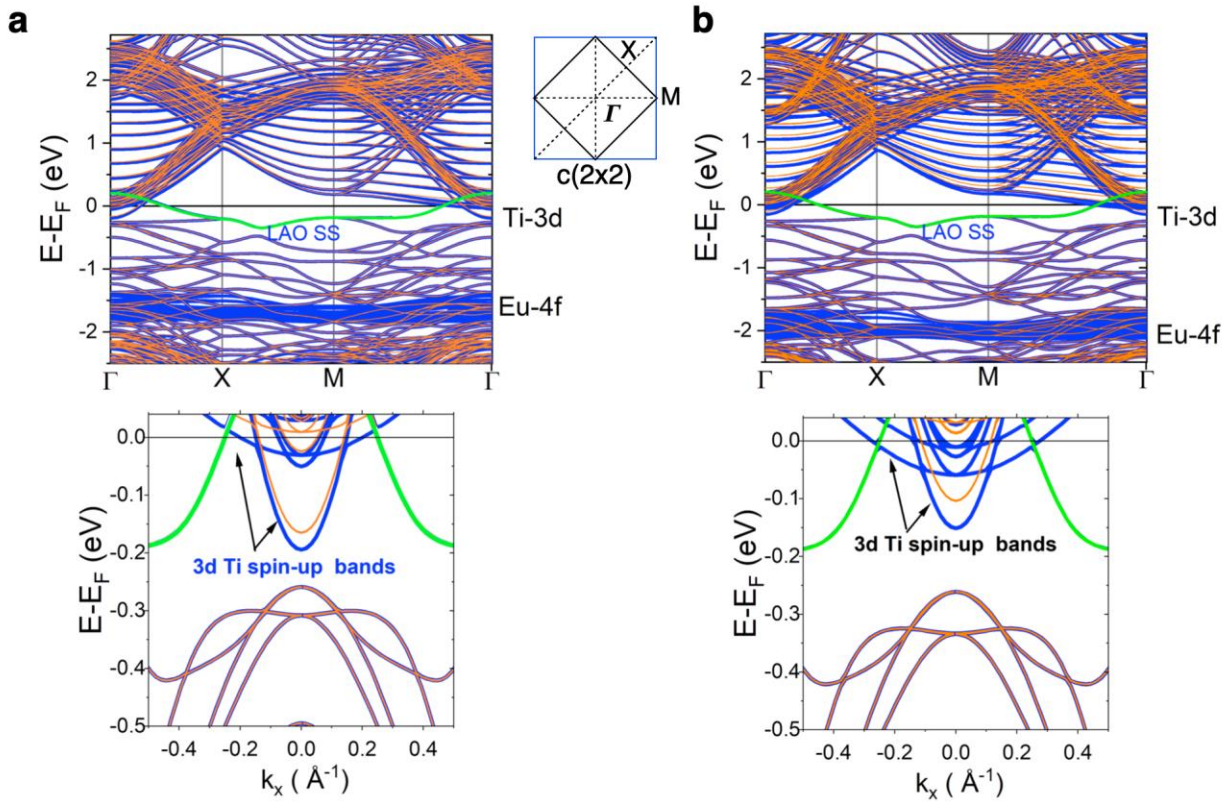

Supplementary Figure 6. **Spin-resolved band structure calculations as function of *U***: (a) Band structure DFT+*U* calculations on LAO/ETO/STO system in the FM ground state (lowest energy configuration) for (a) U=2eV and (b) U=4eV (Spin-up/spin-down bands are denoted in blue/orange). In the upper panels we show the calculations on a large energy range around $E_{F.}$ In the figure Γ-X-M refer to the c(2x2) unit-cell notation (Note that Γ–M in the c(2x2) unit cell is equivalent to Γ–X in the (1x1) unit cell). The LAO surface state (LAO SS) is outlined as a green line. The Eu-*4f* band around -2 eV is fully spin-polarized. (b) Spin-resolved band structure calculations of the Ti-*3d* bands around the Γ-point in a small energy range in the FM (left panel) and AFM (right panel) solutions of the model. Note that in the FM solution, the spin-up $3d_{yz}$ band shift to lower energy and crosses the Fermi level, while the $3d_{xy}$ spin down bands shifts-up, giving rise to an overall spin-polarization of the q2DEG.

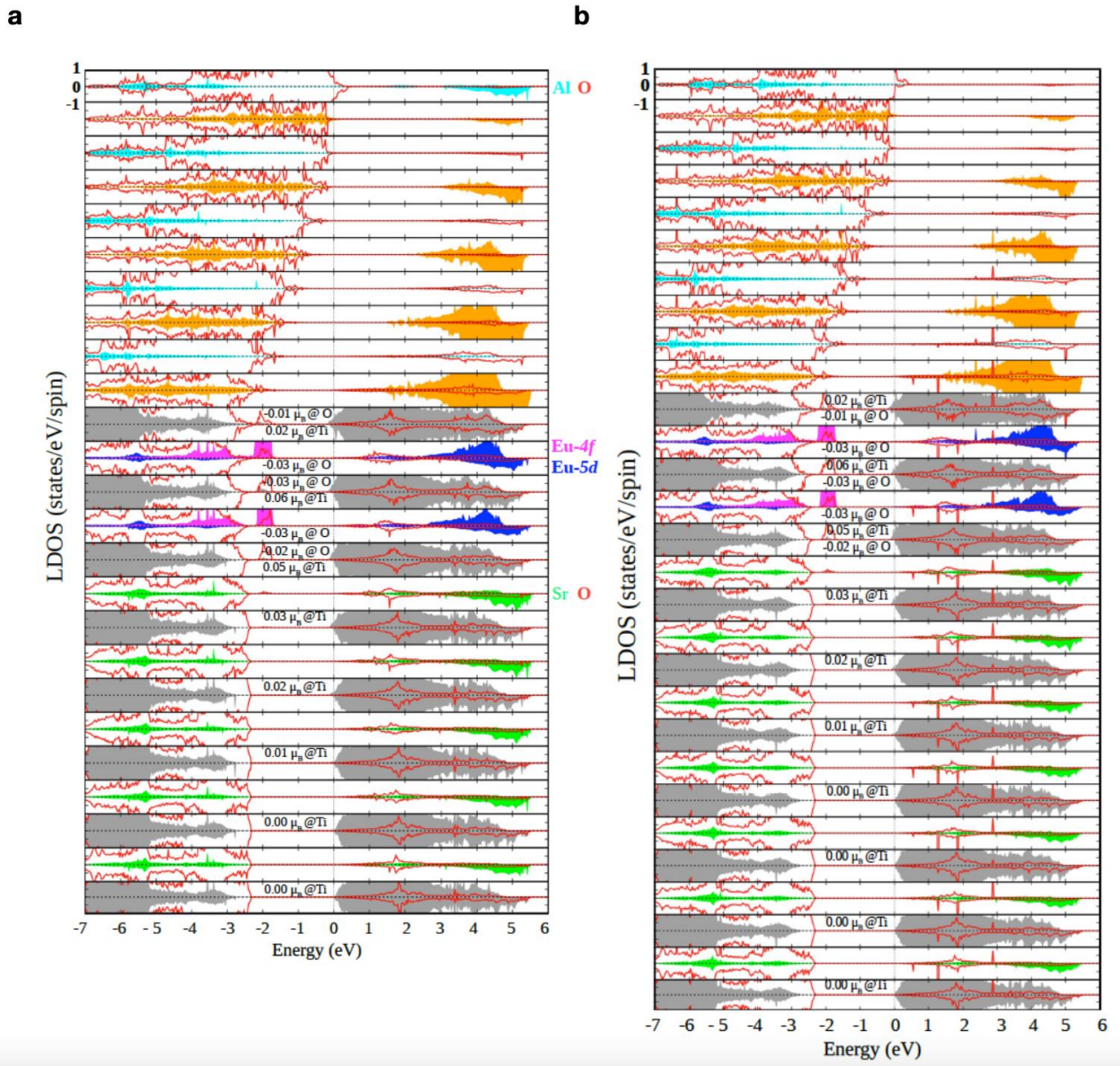

Supplementary Figure 7. Effect of the STO-slabs on DFT+U calculations: Layer and spin-resolved LDOS calculated in the FM ground state by DFT+*U* using different number of STO-slabs. (a) 10.5 STO unit cells; (b) 14.5 STO unit cells (note that the figures show half of the simulation cell).